JOURNAL OF SPACECRAFT AND ROCKETS
Vol. 32, No. 1, January–February 1995

# Numerical Investigation of Supersonic Flows Around a Spiked Blunt Body

Masafumi Yamauchi*
*Tokyo Noko University, Koganei, Tokyo, 184, Japan*
Kozo Fujii†
*Institute of Space and Astronautical Science, Sagamihara, Kanagawa, 229 Japan*
and
Fumio Higashino‡
*Tokyo Noko University, Koganei, Tokyo, 184, Japan*

**In supersonic flow, a spike attached to the nose reduces the drag of a blunt body. In this paper, supersonic flows around a spiked blunt body are numerically simulated to examine the effects of the spike length, Mach number, and angle of attack. Three-dimensional thin-layer compressible Navier–Stokes equations are solved using a high-resolution upwind scheme with LU-ADI time-integration algorithm. The computed results show that the drag of the spiked blunt body is significantly influenced by the spike length, Mach number, and angle of attack. Scales of the separated region are not significantly influenced by the freestream Mach number. For the spiked blunt body at angle of attack, the flowfield becomes complex with spiral flows. The computed results are in reasonable agreement with experimental data.**

## Nomenclature

| | |
|---|---|
| $C_D$ | = drag coefficient |
| $C_P$ | = pressure coefficient, $(p - p_\infty)/q_\infty$ |
| $D$ | = diameter of the blunt body |
| $d$ | = diameter of the spike |
| $L$ | = length of the spike |
| $M$ | = Mach number |
| $P$ | = pressure |
| $q_\infty$ | = dynamic pressure, $\rho_\infty v_\infty^2/2$ |
| $r$ | = coordinate normal to centerline |
| $s$ | = distance from the spike root |
| $v$ | = velocity |
| $x$ | = coordinate of the centerline |
| $\theta$ | = angle measured from the centerline (see Fig. 3), deg |
| $\xi, \eta, \zeta$ | = transformed body-fitted coordinates |
| $\varphi$ | = circumferential angle (see Fig. 3), deg |
| $\rho$ | = density |

*Subscript*

| | |
|---|---|
| $\infty$ | = state of the freestream |

## Introduction

THE drag exerted on a body in supersonic flow is an important problem of aerodynamics. For re-entry into the earth's atmosphere, it is important to control the acceleration of a re-entry capsule by harnessing the drag. Conversely, for escape from the atmosphere, the drag on the body should be reduced. The drag on a blunt body can be reduced by attaching a spike to the nose. At the Institute of Space and Astronautical Science (ISAS), some of the rockets used this technology to reduce the drag on the side booster and thus increase the payload. The spike on the nose is also effective in reducing the heat flux on the surface of a body.

Received Nov. 30, 1992; presented as Paper 93-0887 at the AIAA 31st Aerospace Sciences Meeting, Reno, NV, Jan. 11–14, 1993; revision received Aug. 12, 1993; accepted for publication May 10, 1994. 

*Graduate Student, Department of Mechanical Engineering, Nakacho 2-24-16. Member AIAA.
†Associate Professor, Yoshinodai 3-1-1. Member AIAA.
‡Professor, Department of Mechanical Engineering, Nakacho 2-24-16.

Flowfields around a spiked body were experimentally investigated in the 1950s. For example, flowfields around a spiked blunt body at Mach number 6.8 were experimentally investigated by Crawford[1] in 1959. In this investigation, the effects of the spike length and Reynolds number were examined in detail. According to the results, the drag and the heat flux are reduced when the spike is lengthened, but the drag is not influenced by the spike length when the latter exceeds roughly four times the blunt-body diameter. The investigation also indicated that the drag on the spiked blunt body is influenced by the Reynolds number. In 1960, unsteadiness of the flow caused by the spike on the blunt body nose was studied by Maull[2]; his results indicate that the shock wave around the body oscillates when the nose has a plane shape. Besides these investigations, flows around a spiked body have been investigated by several researchers.[3–6]

In most of the investigations, however, the flows around a spiked body without angle of attack were studied only at hypersonic regimes. Moreover, these investigations are somewhat dated. Though the flowfield has been investigated numerically[7,8] in recent years, physical aspects of flowfields were not discussed in detail. Flowfields around a spiked blunt body display many interesting phenomena that have not been investigated. The features of the flowfield are known conceptually through these investigations. They are characterized by a conical shock wave from the tip of the spike, a separated region in front of the blunt body, and the resulting reattachment shock wave. A schematic diagram of the flowfield is shown in Fig. 1.

In the present paper, supersonic flows over a spiked blunt body are numerically simulated to study the effects of the spike and the mechanism of the drag reduction. The effects of the spike length,

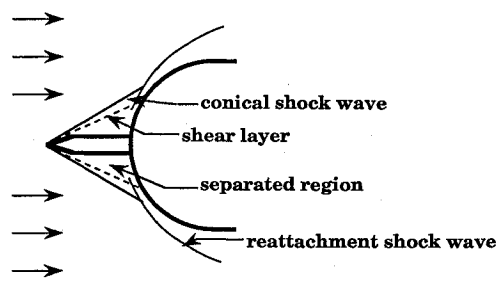


**Fig. 1 Schematic diagram of the flow around a spiked blunt body.**

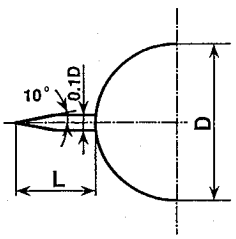


Fig. 2 Shape of the spiked blunt body.

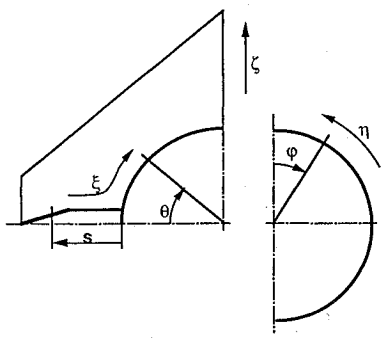


Fig. 3 Local body-fitted coordinates and parameters.

Mach number, and angle of attack are also examined. In case of zero angle of attack, the flow is assumed to be axisymmetric. The axisymmetry of the flow is also discussed. The computed results are compared with experimental data that were obtained with the supersonic wind tunnel at the ISAS as well as those by Crawford.

Since the focus is on the mechanism of the drag reduction and the pattern of the flowfield, the heat flux to the surface of the body is not discussed in the present paper, although it may be important in practical applications. This is one of the topics to be studied in the future.

## Problem Definition and Approach

### Body Configurations

Figure 2 shows the shape of the spiked blunt body used in the present study. The configuration of the spiked body is the same as in the model that was investigated by Crawford.[1] The model is axisymmetric, and the main blunt body has a hemispherical nose whose diameter is defined to be $D = 1.0$. The spike consists of a conical part and the following cylindrical part. The angle of the cone is 10 deg, and the diameter of the cylinder, $d$, is $0.1D$. Spike lengths of $L = 0.5D$, $1.0D$, and $2.0D$ are considered. The model in the experiment by Crawford has a cylindrical afterbody that follows the hemispherical nose, but it is not included in the present study.

### Flow Conditions

Freestream Mach numbers are 6.80, 4.15 and 2.01, Reynolds number is 140,000 based on the diameter of the hemispherical nose, and the flow is assumed to be laminar, consistent with Ref. 1. The Mach numbers are selected for comparison with experiments.

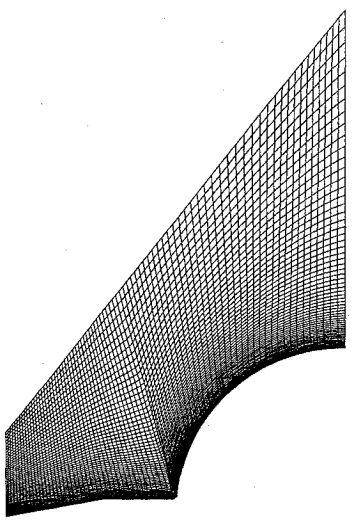

a) Grid surface of $L/D$ = 0.5

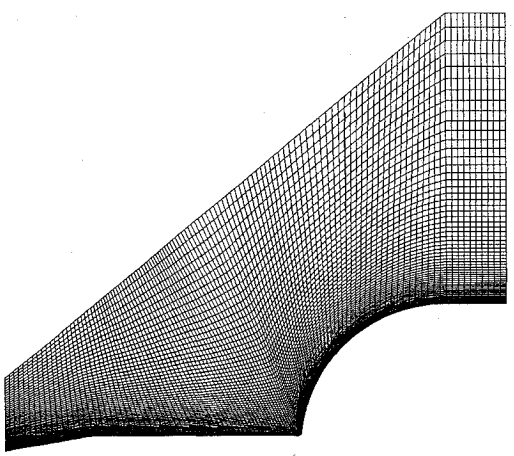

b) Grid surface of $L/D$ = 1.0

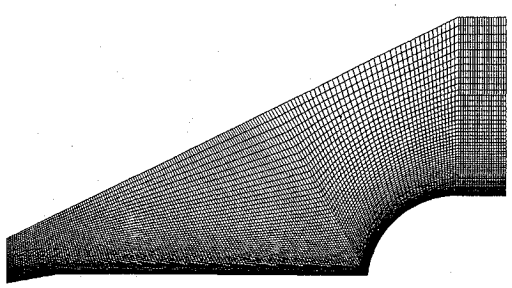

c) Grid surface of $L/D$ = 2.0

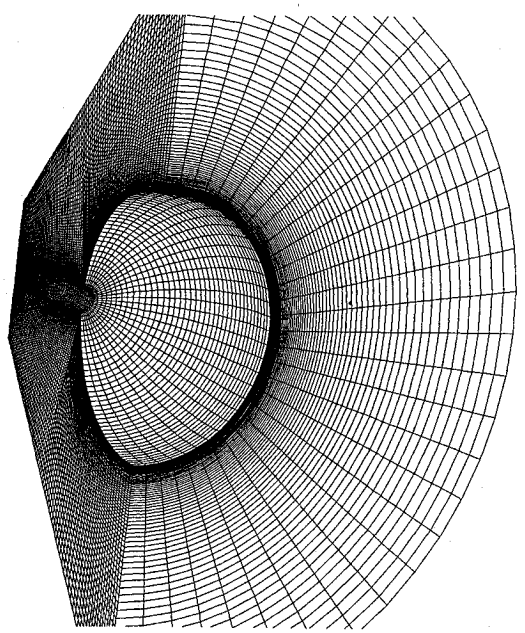

d) Grid for three-dimensional computation

Fig. 4 Computational grids.

The flow is also assumed to be axisymmetric at zero angle of attack. The flow around the spiked blunt body at angle of attack is simulated only at Mach number 6.80 and 10-deg angle of attack. To examine the validity of the axisymmetric assumption, the flow around the spiked blunt body at 0 angle of attack is also simulated without the axisymmetry assumption, using the same grid as for 10-deg angle of attack.

### Computational Grids

The local body-fitted coordinates of the spiked blunt body in the simulation are indicated in Fig. 3. The direction along the body surface is $\xi$, the circumferential direction is $\eta$, and the outward direction from the body is $\zeta$. The $\eta$ = constant grid surfaces for $L/D = 0.5$, 1.0, and 2.0 are shown in Figs. 4a–4c, respectively. The grid of $L/D = 0.5$ has 81 points in the $\xi$ direction and 81 points in the $\zeta$ direction. The grid points for spike lengths of 1.0 and 2.0 are $121 \times 81$ and $191 \times 81$, respectively. The two-dimensional grid surfaces described above are rotated around the $x$ axis, and three grid planes are prepared at 3-deg intervals. Two of the outer planes are used for imposing the boundary conditions in the circumferential direction, and only one middle plane is solved. Three-dimensional Navier-Stokes equations are used for all solutions, including the axisymmetric cases. By imposing the solution at the middle plane onto the outer planes, the solutions at all the three planes become the same in the steady-state solution, which satisfies the assumption of axisymmetric flow.

The computational grid for the fully three-dimensional simulation covers half of the whole flowfield, assuming a plane of symmetry. The grid has 33 points in the $\eta$ direction. The overall view of the grid is shown in Fig. 4d.

### Numerical Method

The governing equations of the numerical simulations are three-dimensional thin-layer compressible Navier-Stokes equations, which are written in strong-conservation-law form in a generalized coordinate system. The equations are solved using a high-resolution upwind scheme[9] with LU-ADI time integration.[10] Local time stepping is used, since the flow is assumed to be steady. Turbulence models are not used, since laminar flow is indicated in the experiment.[1]

### Initial Condition and Boundary Conditions

The initial flowfield is set to be freestream everywhere, and an impulsive start is applied for the cases at Mach numbers 2.01 and 4.15. For the high-Mach-number flow simulations at $M = 6.80$, the computation may possibly be unstable when an impulsive start is applied. The Mach number is gradually increased at the inflow boundary until it reaches the freestream Mach number, 6.80.

All variables are extrapolated at the outflow boundary, and the nonslip wall condition is applied on the surface of the body. For the axisymmetric simulations, the axisymmetric condition is satisfied by imposing the flow variables at the middle plane ($\eta = 2$) on those at the boundaries ($\eta = 1$ and 3). For the fully three-dimensional computations, flow symmetry is imposed on the symmetry plane and only half of the whole three-dimensional flow field is solved.

## Results and Discussion

### Flow Characteristics

Figures 5a and 5b show the computed flowfield using the axisymmetric assumption for the spike length of $L/D = 0.5$, at a freestream Mach number of 6.80 and 0 angle of attack. Figure 5a is the density contour plot, and Fig. 5b is the velocity-vector plot near the base of the spike. In these figures, interaction between the oblique (conical) shock wave from the tip of the spike and the reattachment shock wave is observed. The reflected shock wave and the shear layer from the interaction are seen behind the reattachment shock wave. A large separated region is observed in front of the blunt body in Fig. 5b, and the shear layer (the boundary of the separated region over the spike) is clearly seen below the conical shock wave in Fig. 5a. In the separated region, a number of vortices exist and the velocity magnitude is very low, as is shown in Fig. 5b.

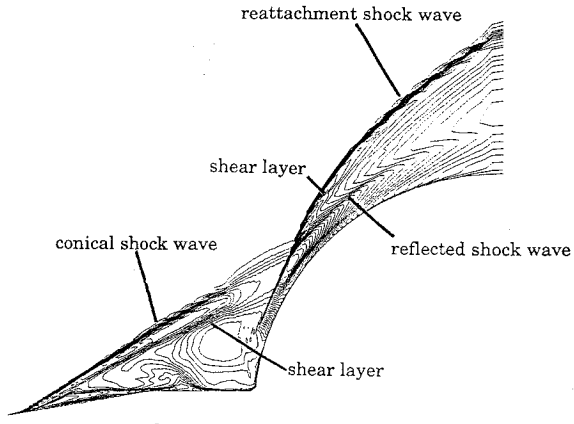


**a) Density contour plot**

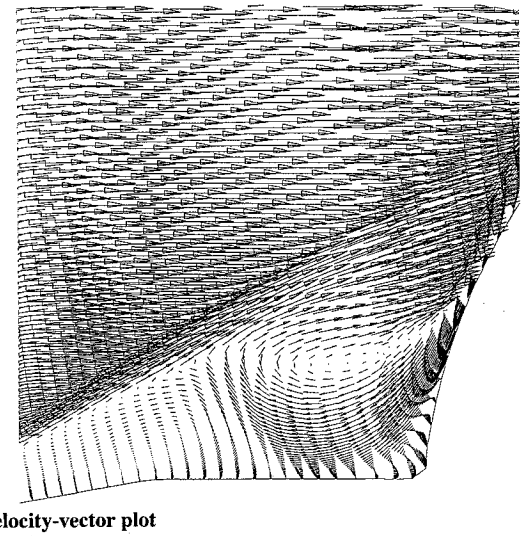

**b) Velocity-vector plot**

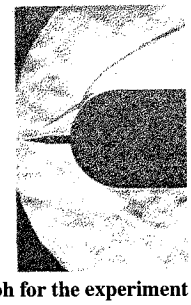

**c) Schlieren photograph for the experiment (Ref. 1), $Re = 0.14 \times 10^6$**

**Fig. 5 Flowfield for the spiked blunt body with $L/D = 0.5$ at $M = 6.80$.**

Good agreement is obtained between the computed flowfield and the schlieren photograph from the experiment[1] shown in Fig. 5c.

The computed flowfields for spike lengths $L/D = 1.0$ and 2.0 are shown in Figs. 6 and 7. Figures 6a and 7a are the density contour plots, and Figs. 6b and 7b are the velocity-vector plots in front of the nose. The flow patterns are the same as for $L/D = 0.5$. With a longer spike, the angle of the oblique shock wave from the spike tip is decreased and flow separation occurs slightly downstream. Since the reattachment point has moved backward, the scale of the separated region is increased. The angle of the conical shock wave depends on the angle of the shear layer, which gives the effective body geometry to the outer freestream. Both of these computed flowfields also agree with the schlieren photographs taken in the experiment[1] (see Figs. 6c and 7c). Note that the computed results shown in Figs. 5–7 are the solutions at one particular time. Flow unsteadiness and the time-averaged solutions will be discussed in the next section.

Figures 8 and 9 show the computed flowfields at Mach numbers 4.15 and 2.01, respectively. The flow field at Mach number 4.15 also

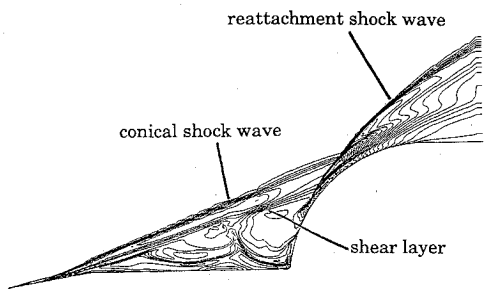


a) Density contour plot

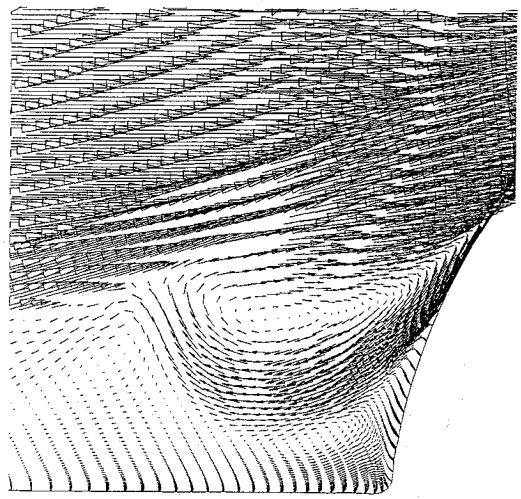

b) Velocity-vector plot

c) Schlieren photograph for the experiment (Ref. 1), $Re = 0.33 \times 10^6$

**Fig. 6 Flowfield for the spiked blunt body with $L/D$ = 1.0 at $M$ = 6.80.**

shows a conical shock wave from the spike tip, a separated region in front of the blunt body, and the resulting reattachment shock wave. The flow pattern is similar to that of the Mach-number-6.80 solution. However, the conical shock wave is distorted. This may be caused by the unsteadiness of the flow, which is discussed later. The shape of the shock wave at Mach number 2.01 is different from that at Mach number 6.80 or 4.15. In Fig. 9a, the shock wave from the tip of the spike merges into the reattachment shock wave over the blunt body. Though a shear layer is not clearly seen in Fig. 9a, the velocity-vector plot in Fig. 9b indicates that the shear layer exists above the separation vortex in the separated region.

According to these computed flowfields, the angle of the conical shock wave is much larger than that for a single cone of 10 deg. The reason is that the recirculating region behaves as if it were a body boundary. As a result, the flow around the spike becomes similar to the flow around a single cone of more than 10 deg. The scale of the separated region in front of the blunt nose is not significantly influenced by the freestream Mach number.

The computed flowfield at Mach numbers 4.15 and 2.01 qualitatively agrees with the photographs taken in the present authors' experiment, shown in Figs. 8c and 9c, although the Reynolds number is one order of magnitude larger in the experiment.

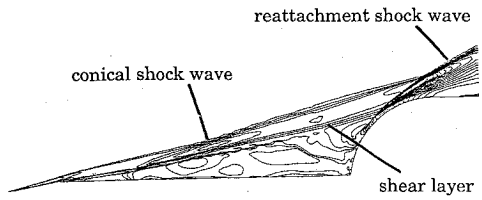


a) Density contour plot

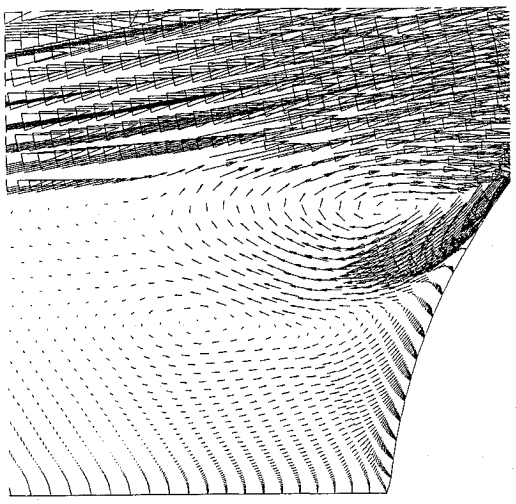

b) Velocity-vector plot

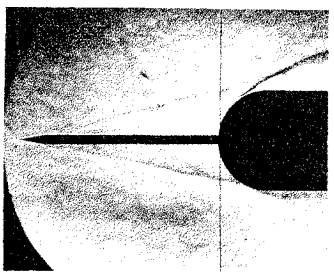

c) Schlieren photograph for the experiment (Ref. 1), $Re = 0.15 \times 10^6$

**Fig. 7 Flowfield for the spiked blunt body with $L/D$ = 2.0 at $M$ = 6.80.**

## Pressure Distribution and Flow Unsteadiness

Figure 10 shows the pressure distribution on the body surface with the freestream Mach number as a parameter. At any Mach number, a wavy pattern is observed in the pressure distribution in the spike region. The peak and global pressure levels on the blunt-body surface are reduced with decreasing freestream Mach number, corresponding to the trends in pressure on a nonspiked hemisphere. The location of the pressure peak on the surface of the spiked blunt body is located about $\theta = 40$ deg at all the Mach numbers. This is the reattachment point of the separated flow over the spike. The shear layer created on the spike region passes through the reattachment shock wave and impacts the blunt body surface, resulting in the high pressure peak.

The pressure distribution on the surface for spike lengths $L/D$ = 0.5, 1.0, and 2.0 are compared in Fig. 11. The peak pressure decreases as the spike length is increased. Figures 5b–7b indicate that a longer spike creates a larger separated region in front of the blunt body. As a result, the reattachment point of the separated region and the location of the maximum-pressure point move downstream for the longer spike. The drag on the blunt body is expected to be significantly influenced by the spike length.

In the simulations described, strict steady-state solutions were not obtained in all cases. The pressure distributions in Figs. 10 and 11 are the instantaneous distributions. Figures 5–9 show that the shock waves from the spike tip are distorted by the unsteadiness of the flow. The conical shock wave is a little distorted for spike length

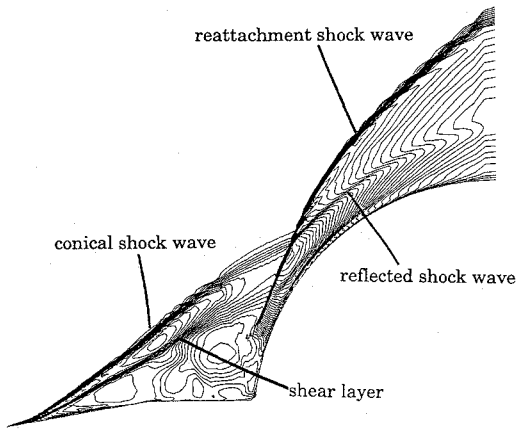


a) Density contour plot

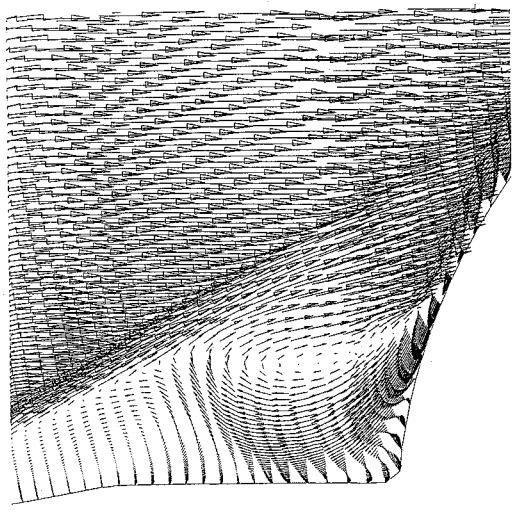

b) Velocity-vector plot

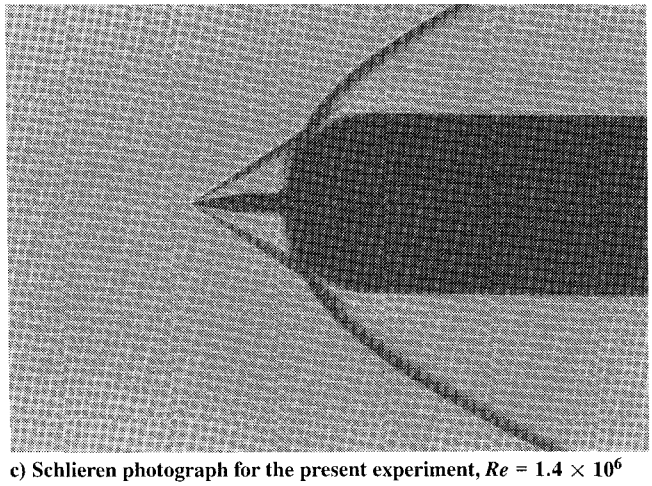

c) Schlieren photograph for the present experiment, $Re = 1.4 \times 10^6$

**Fig. 8 Flowfield for the spiked blunt body with $L/D = 0.5$ at $M = 4.15$.**

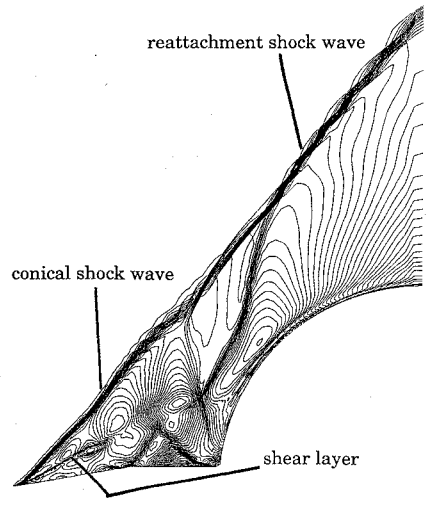


a) Density contour plot

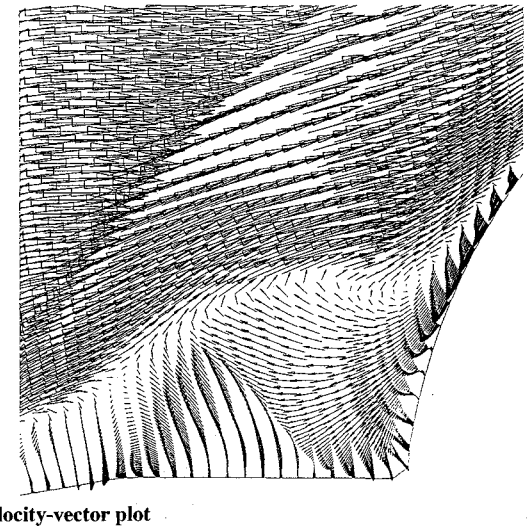

b) Velocity-vector plot

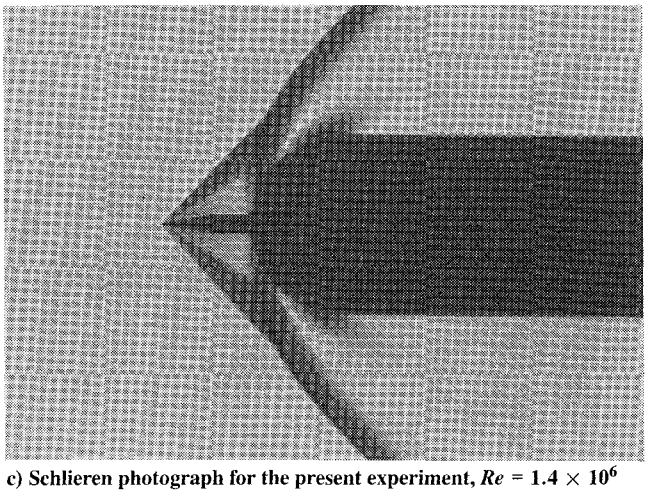

c) Schlieren photograph for the present experiment, $Re = 1.4 \times 10^6$

**Fig. 9 Flowfield for the spiked blunt body with $L/D = 0.5$ at $M = 2.01$.**

$L/D = 0.5$ and is highly distorted for $L/D = 1.0$ or 2.0, depending on time. This phenomenon may be caused by the unsteady vortices in the separated region. The shape of the conical shock wave at low Mach numbers also depends on time.

The drag-coefficient history of the spiked blunt body with spike length $L/D = 0.5$ is shown in Fig. 12. The coefficient changes periodically in all the figures. Since these computations do not have time accuracy on account of the space-variable time stepping, unsteadiness of the flow cannot be discussed quantitatively. However, it is interesting that the drag changes periodically even with local time stepping. In the present simulations, the grid cell size does not change appreciably in the inviscid flow region. The simulations may be fairly time-accurate for the large-scale flow structures.

Figures 13a–13c show the averaged flow fields at three Mach numbers for spike length $L/D = 0.5$. The average is taken for a few cycles of the drag history. Straight conical shock waves

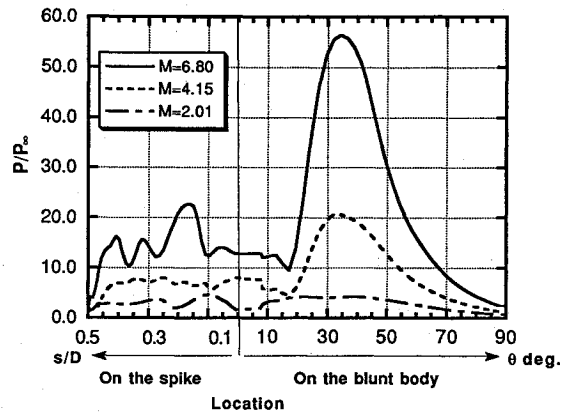


**Fig. 10 Pressure distributions with the freestream Mach number as a parameter: $L/D = 0.5$.**

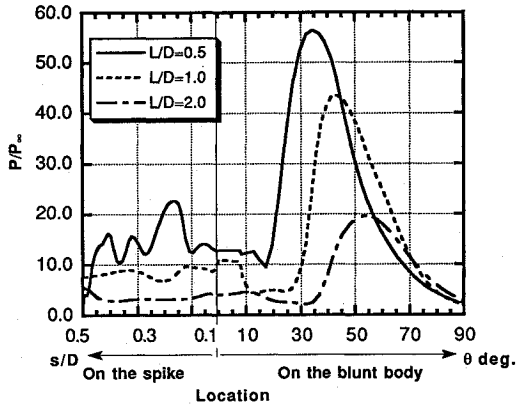


**Fig. 11 Pressure distributions with the spike length as a parameter: $M = 6.80$.**

are observed in the averaged flowfields. The flowfields agree well with the photographs (Figs. 5c, 8c, and 9c) taken in the experiments.

Figures 14a–14c are plots of the averaged pressure distribution on the surface of the blunt body with the spike of $L/D = 0.5$ along with the experimental data at Mach numbers 6.80, 4.15, and 2.01, respectively. Also plotted are the pressure distributions for the nonspiked blunt body. The pressure distributions in the spike region are flatter than those in Fig. 10 because unsteady motion of the vortices in the separated region is averaged.

At a freestream Mach number of 6.80, the computed pressure distribution shows fairly good agreement with the experimental data.[1] However, the location of the maximum pressure is shifted slightly forward in the computation. At a Mach number of 4.15, the computed pressure distribution shows essentially the same result as the experiment, but again it is shifted slightly forward. The reason proposed is that the reattachment point is shifted forward by the same distance as of the initial point of the separation on the spike. At a Mach number of 2.01, the pressure distribution again agrees well with the experiment. The peak pressure on the surface of the spiked blunt body is much lower than that on the nonspiked blunt body. Therefore, drag reduction is expected in all the cases.

Since the peak pressure is located at about $\theta = 40$ deg at all flow conditions, the scale of the separated region is not much influenced by the Mach number. The conical shock wave from the spike tip and the reattachment shock wave on the blunt body interact with each other at small relative angles, and the resulting shear layer and the reflected shock wave remain away from the blunt body, as is seen in Figs. 5a, 8a, and 9a. Therefore, the pressure distribution on the surface of the blunt body is not directly influenced by the conical-shock–reattachment-shock interaction. However, the peak pressure on the blunt-body surface reflects the fact that the pressure

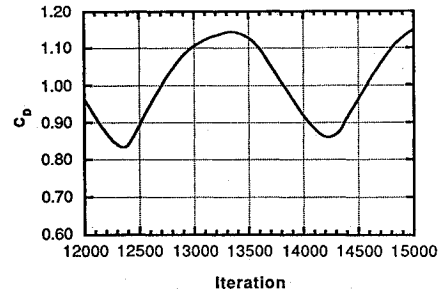


a) $M = 2.01$

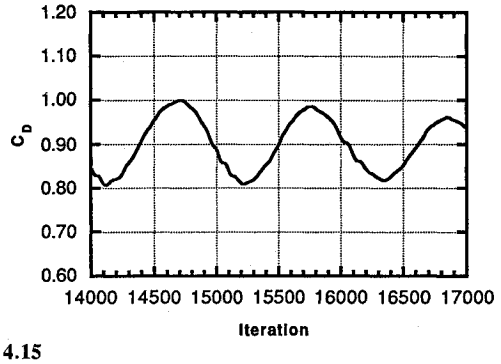


b) $M = 4.15$

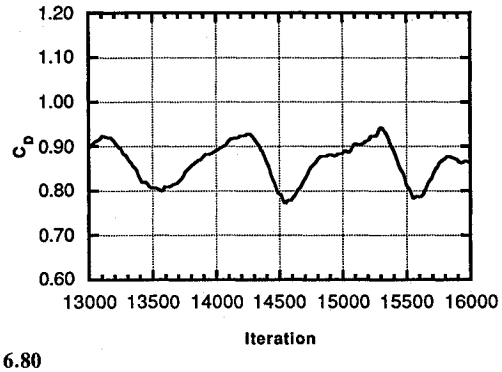


c) $M = 6.80$

**Fig. 12 Drag-coefficient iteration history: $L/D = 0.5$.**

is increased when the shear layer passes through the reattachment shock wave. Thus, the surface pressure is indirectly influenced by the conical-shock–reattachment-shock interaction, although the reflected shock wave does not impact on the body surface. The pressure distributions on the blunt-body surface are mainly governed by the shear layer created by the spike tip, the recirculating region in front of the blunt body, and the resulting reattachment shock wave.

### Axisymmetry of the Flow

The fully three-dimensional computations at zero angle of attack provide essentially the same result as that obtained with the axisymmetric assumption, as is shown in Figs. 15a–15c. These figures show the density contour plots and the velocity vector plots on the planes of $\varphi = 0$, 90, and 180 deg, respectively. The axisymmetry of the flow is recognized by the fact that the flowfield on these planes are globally similar to each other. However, the interaction between the conical shock wave and the reattachment shock wave is a little stronger than that under the axisymmetric condition. Figure 15d shows the velocity vectors in the crossflow plane at the separated region (front view), and Fig. 15e shows both the density contour plots on the symmetry planes and the streamlines near the spike tip and the separated region. As is shown in Fig. 15d, weak crossflow exists even at zero angle of attack. The flow in the separated region seems to be unsteady. On the other hand, the flow outside the separated

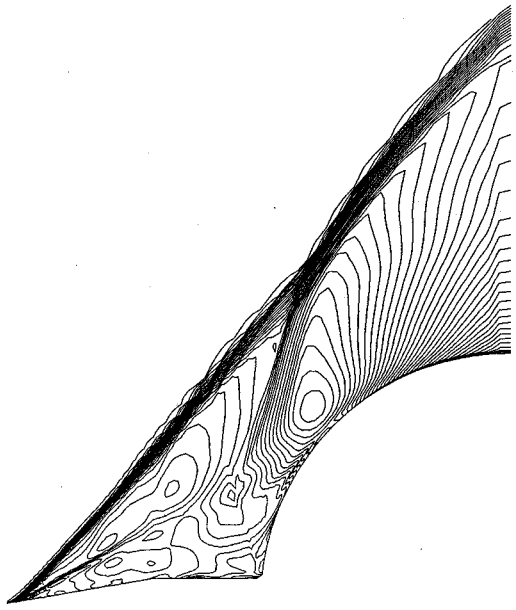

a) Density contour plot at $M$ = 2.01

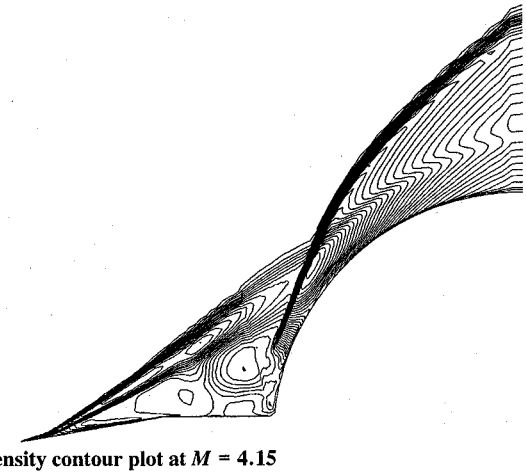

b) Density contour plot at $M$ = 4.15

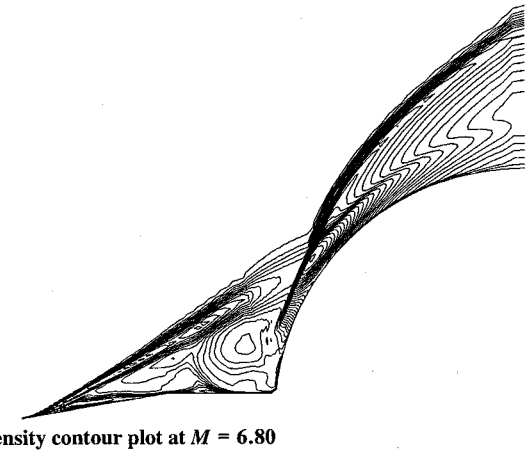

c) Density contour plot at $M$ = 6.80

**Fig. 13 Averaged flowfields for $L/D$ = 0.5.**

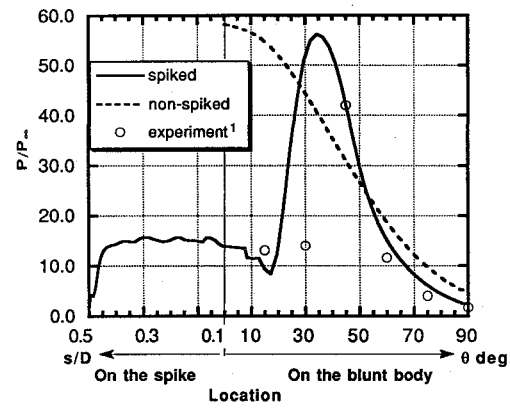


a) $M$ = 6.80

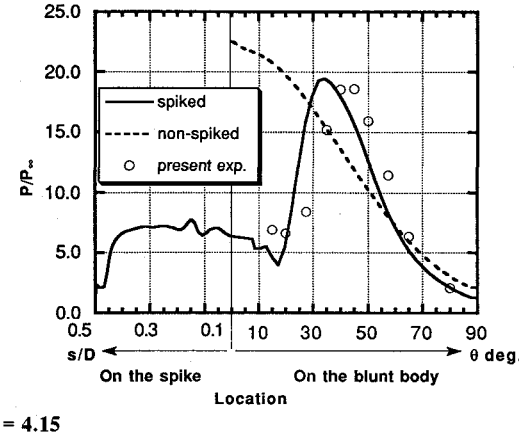


b) $M$ = 4.15

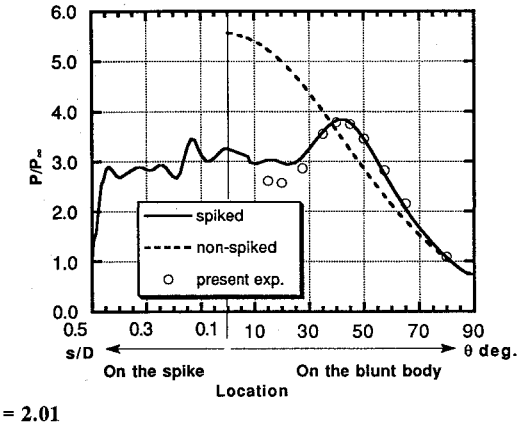


c) $M$ = 2.01

**Fig. 14 Averaged pressure distributions on the spiked and nonspiked blunt-body surface: $L/D$ = 0.5.**

region (shown in Figs. 15d and 15e) indicates that the axisymmetric condition is globally satisfied.

Figure 16 shows the pressure distributions on the body surface for $\varphi = 0$, 90, and 180 deg at zero angle of attack. The results are similar for all planes, since the flowfield is basically axisymmetric except for the separated region in front of the body. The pressure distributions are the same as for the axisymmetric condition, and the location of the pressure peak is also about $\theta = 40$ deg (see Fig. 10a). As is observed in Figs. 15d and 16, the streamlines hit the body at the peak pressure point.

From the observations above, the global flowfield for the three-dimensional solution at zero angle of attack can be considered equivalent to the computed results using the axisymmetric boundary condition.

**Effects of Angle of Attack**

The flow around the spiked blunt body at 10-deg angle of attack is described. Figures 17a–17c show the density contour and the velocity-vector plots in the three streamwise planes corresponding to $\varphi = 0$, 90, and 180 deg, respectively. In Fig. 17a, the shock wave from the tip of the spike merges into the reattachment shock wave of the blunt body. In the other planes (Figs. 17b and 17c), the flow patterns are similar to the results obtained for 0 angle of attack. The

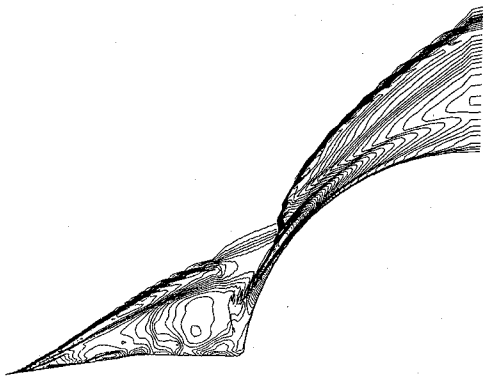

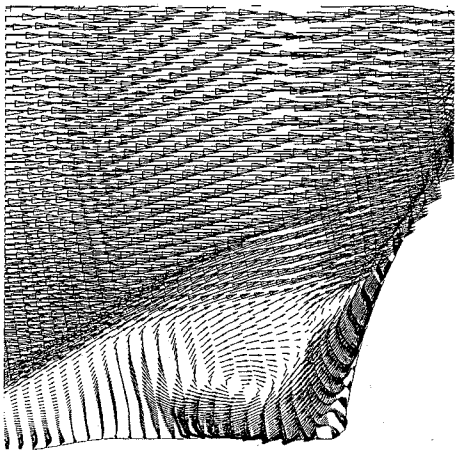

a) Density contour and velocity-vector plots on the $\varphi$ = 0 plane

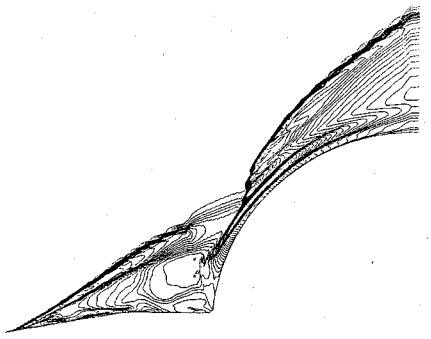

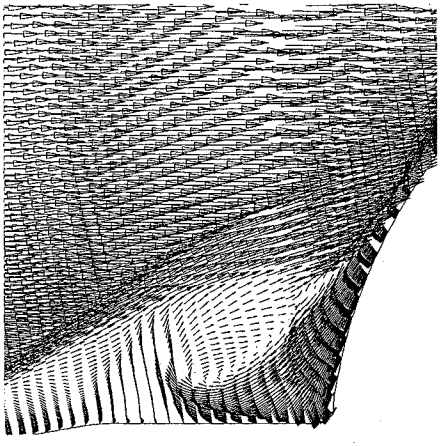

c) Density contour and velocity-vector plots on the $\varphi$ = 180-deg plane

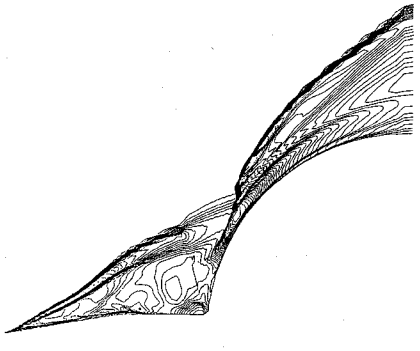

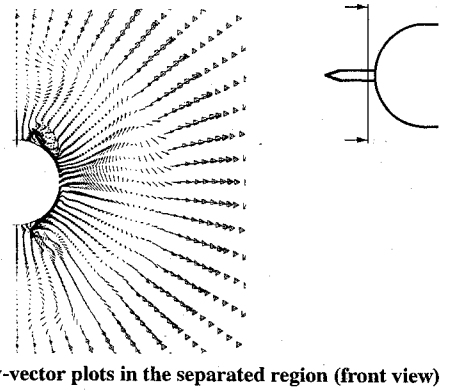

d) Velocity-vector plots in the separated region (front view)

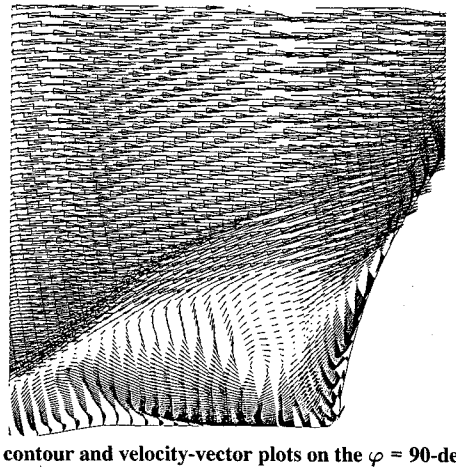

b) Density contour and velocity-vector plots on the $\varphi$ = 90-deg plane

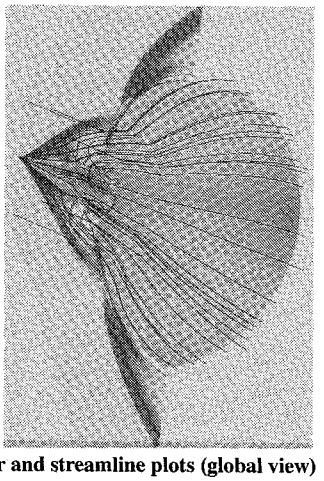

e) Density contour and streamline plots (global view)

**Fig. 15 Flowfield for the fully three-dimensional computation at $M$ = 6.80 and 0 angle of attack: $L/D$ = 0.5.**

**Table 1 Drag coefficients for the spiked blunt body with $L/D = 0.5$ at $M = 6.80$**

a) Effect of the angle of attack on the drag coefficients of the spiked blunt body (3-D computation)

| Angle of attack, deg | $C_D$ |
|---|---|
| 0 | 0.867 |
| 10 | 0.851 |

b) Comparison of the drag coefficients of the axisymmetric and fully three-dimensional computations

| Axisymmetric | 3-D |
|---|---|
| 0.861 | 0.867 |

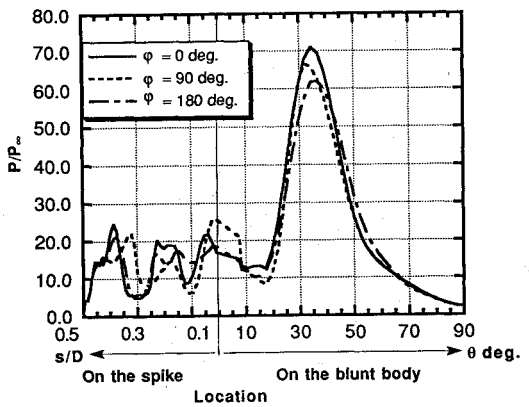


**Fig. 16 Pressure distributions for the fully three-dimensional computation at $M = 6.80$ and 0 angle of attack: $L/D = 0.5$.**

vortices in the separated region are stronger than those at 0 angle of attack.

Figure 17d shows the velocity vectors around the blunt body (front view), and Fig. 17e shows the streamlines and the density contour plots in the symmetry plane. Vertical flows moving up along the blunt-body nose are shown in Fig. 17d. These spiral flows are indicative of necklace vortices, because the upward crossflow passes the spike vertically. Similar flow patterns were observed in an experiment for a different type of a spiked blunt body, and the flow features have been explained in Ref. 11.

Figure 18 shows the pressure distributions on the surface at 10-deg angle of attack. Comparison of Figs. 16 and 18 indicates that the pressure distributions on the surface of the body for 10-deg angle of attack are significantly different from that for 0 angle of attack. The pressure peak on the lower surface ($\varphi = 180$ deg) of the body is very high because the shear layer impacts the body almost vertically. Conversely, the pressure level on the upper surface ($\varphi = 0$) is low because the pressure on the body is not influenced by the shear layer.

**Mechanism of Drag Reduction**

Drag coefficients for the spiked blunt body and the nonspiked blunt body were computed from the averaged flow fields. Note that both the pressure and viscous contributions are included in the drag coefficient, but the contribution from the base region is not included. In other words, the pressure in the base region is assumed to have the freestream value when computing the drag coefficient. Effects of the spike on drag is illustrated in Fig. 19 by the ratio of the drag coefficients for the spiked and non-spiked blunt bodies as a function of Mach number for the $L/n = 0.5$ spike length. The spiked blunt body drag coefficient is smaller than the corresponding nonspiked-blunt-body drag coefficient at any Mach number. As is shown in Table 1a, the drag coefficient of the spiked blunt body at 10-deg angle of attack is essentially the same as that at zero angle of attack. In Table 1b, the drag coefficient from the axisymmetric computation is compared with that from the fully three-dimensional computation. The result shows almost the same value. Therefore, a spike on the

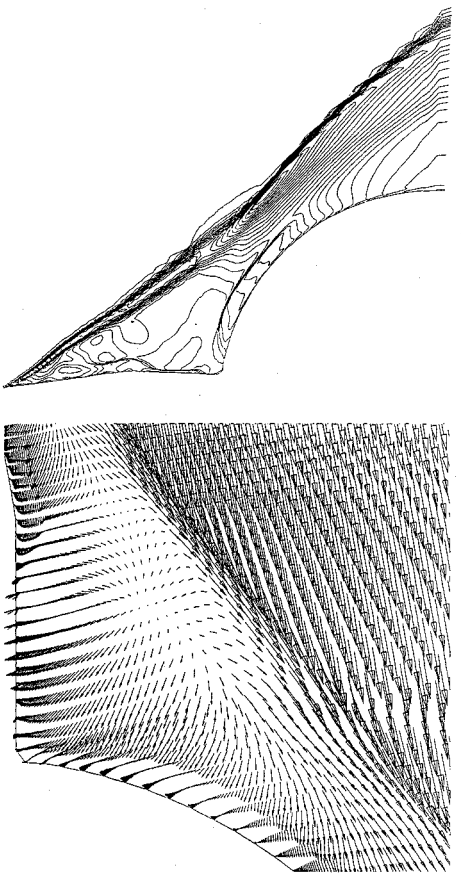

a) Density contour and velocity-vector plots on the $\varphi = 0$ plane

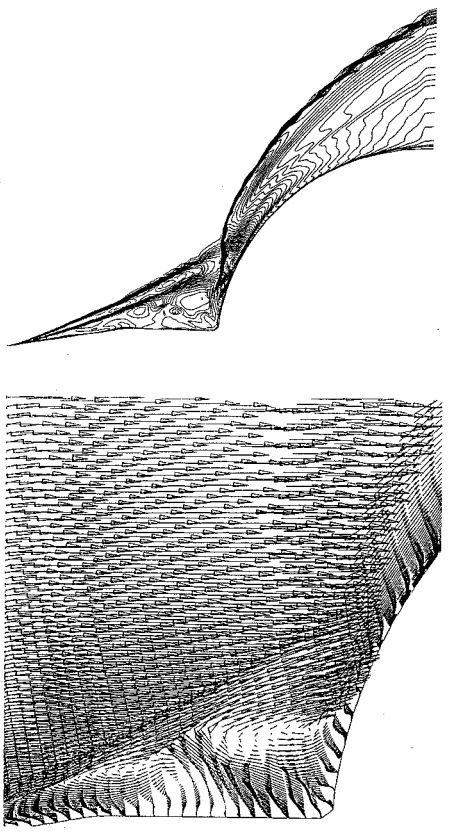

b) Density contour and velocity-vector plots on the $\varphi = 90$-deg plane

**Fig. 17 Flowfield for the fully three-dimensional computation at $M = 6.80$ and 10-deg angle of attack: $L/D = 0.5$.**

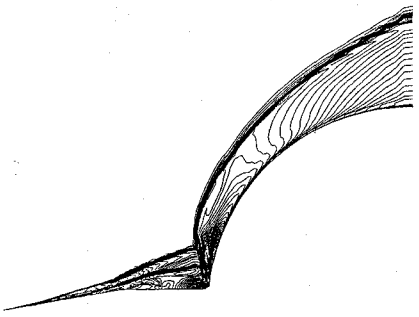

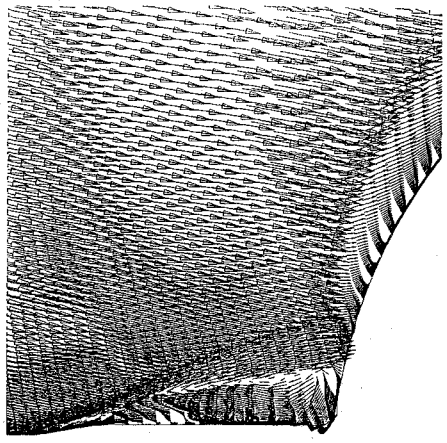

c) Density contour and velocity-vector plots on the $\varphi$ = 180-deg plane

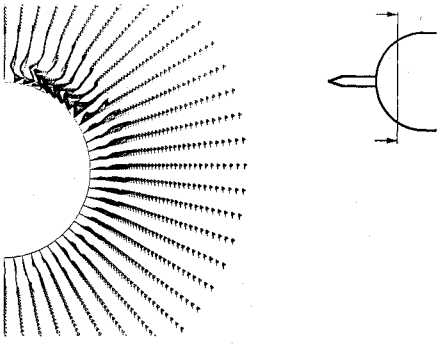

d) Velocity-vector plots at the blunt body (front view)

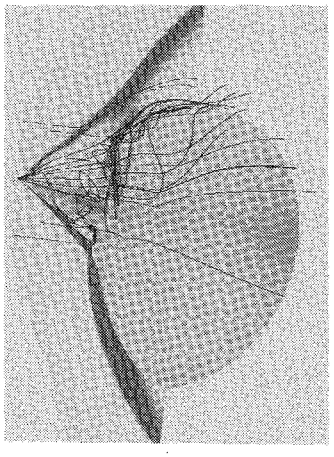

e) Density contour and streamline plots (global view)

Fig. 17 (Continued) Flowfield for the fully three-dimensional computation at $M$ = 6.80 and 10-deg angle of attack: $L/D$ = 0.5.

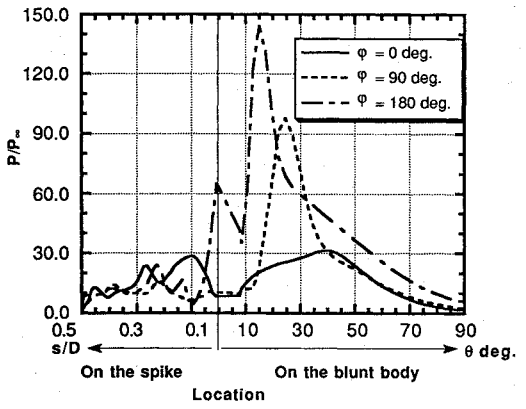


Fig. 18 Pressure distributions for the fully three-dimensional computation at $M$ = 6.80 and 10-deg angle of attack: $L/D$ = 0.5.

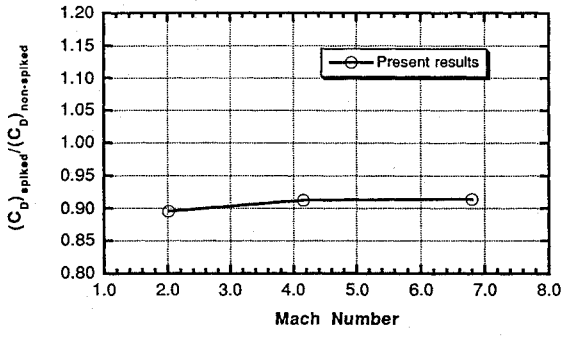


Fig. 19 Drag-coefficient ratio for the spiked and nonspiked blunt bodies with the freestream Mach number as a parameter: $L/D$ = 0.5.

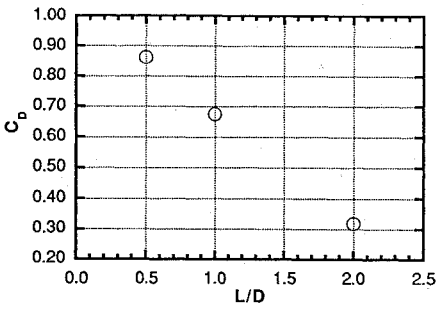


Fig. 20 Drag coefficients for the spiked blunt body at $M$ = 6.80 with the spike length as a parameter.

nose is effective in drag reduction even when the freestream Mach number is varied or the blunt body is at an angle of attack.

The key feature for the drag reduction is the pressure distribution on the body surface, particularly near the nose. For the spiked blunt body, the pressure near the nose is very low because of the separation existing under all conditions.

The drag coefficient vs the spike length is presented in Fig. 20. The drag is reduced when the spike is lengthened. Figure 11 showed that the pressure is lower on the surface of the body with a longer spike, thereby reducing the drag. The flow around a spiked blunt body becomes similar to the flow around a single cone of more than 10 deg. The drag on a cone is smaller than that on a blunt body. Thus, the drag is reduced because of the separated region created by the spike on the nose.

## Concluding Remarks

Supersonic flows around a spiked blunt body have been simulated numerically. The flowfields around the spiked blunt body at zero angle of attack under various conditions are all characterized by a conical shock wave, a separated region in front of the blunt body, and the resulting reattachment shock wave for several Mach numbers and spike lengths. The drag is greatly influenced by the spike length,

which affects the pressure on the surface in the separated region on the front face of the blunt body. The area of the separated region is extended by the longer spike, but is not much influenced by the Mach number. In the separated region, the pressure level becomes low, which causes the drag reduction.

When the angle of attack is 10 deg, spiral flow occurs along the blunt-body nose due to the spike. The pressure distributions of the spiked blunt body at 10-deg angle of attack are remarkably different from those at zero angle of attack, but the drag coefficient is essentially the same. The drag is also reduced at this angle of attack.

In general, good agreement is obtained between the present computations and the available experimental data.

## References

[1]Crawford, D. H., "Investigation of the Flow over a Spiked-Nose Hemisphere-Cylinder at a Mach Number of 6.8," NASA TN D-118, Dec. 1959.

[2]Maull, D. J., "Hypersonic Flow over Axially Symmetric Spiked Bodies," *Journal of Fluid Mechanics*, Vol. 8, Pt. 4, 1960, pp. 584–592.

[3]Bogdonoff, S. M., and Vas, I. E., "Preliminary Investigations of Spiked Bodies at Hypersonic Speeds," *Journal of the Aero. Space Sciences*, Vol. 26, No. 2, 1959, pp. 65–74.

[4]Wood, C. J., "Hypersonic Flow over Spiked Cones," *Journal of Fluid Mechanics*, Vol. 12, Pt. 4, 1962, pp. 614–627.

[5]Thurman, W. E., "A Flow-Separation Spike for Hypersonic Control of a Hemisphere-Cylinder," *AIAA Journal*, Vol. 2, No. 1, 1964, pp. 159–161.

[6]Hutt, G. R., and East, R. A., "Static and Dynamic Pitch Stability of a Blunted Cone with Forward Facing Aerodynamic Spike in Hypersonic Flow," *The Aeronautical Journal*, Vol. 89, No. 888, 1985, pp. 307–314.

[7]Shoemaker, J. M., "Aerodynamic Spike Flowfields Computed to Select Optimum Configuration at Mach 2.5 with Experimental Validation," AIAA Paper 90-0414, Jan. 1990.

[8]Fujita, M., and Kubota, H., "A Simulation of Flow Separation Effects Ahead of Blunt Bodies," *A Collection of Technical Papers, 4th International Symposium on CFD*, Vol. 1, Univ. of California, Davis, CA, 1991, pp. 359–364.

[9]Fujii, K., and Obayashi, S., "High-Resolution Upwind Scheme for Vortical-Flow Simulations," *Journal of Aircraft*, Vol. 26, No. 12, 1989, pp. 1123–1129.

[10]Obayashi, S., Matsushima, K., Fujii, K., and Kuwahara, K., "Improvement in Efficiency and Reliability for Navier-Stokes Computations Using the LU-ADI Factorization Algorithm," AIAA Paper 86-0338, Jan. 1986.

[11]Guenther, R. A., and Reding, J. P., "Fluctuation Pressure Environment of a Drag Reduction Spike," *Journal of Spacecraft and Rockets*, Vol. 14, No. 12, 1977, pp. 705–710.